The Astrophysical Journal Letters, 978:L5 (11pp), 2025 January 01 https://doi.org/10.3847/2041-8213/ad9aa8

Dark Matter Distinguished by Skewed Microlensing in the "Dragon Arc"

Tom Broadhurst[1,2,3], Sung Kei Li[4], Amruth Alfred[4], Jose M. Diego[5], Paloma Morilla[2,1], Patrick L. Kelly[6], Fengwu Sun[7,8], Masamune Oguri[9,10], Hayley Williams[6], Rogier Windhorst[11], Adi Zitrin[12], Katsuya T. Abe[9], Wenlei Chen[13], Liang Dai[14], Yoshinobu Fudamoto[9], Hiroki Kawai[15,9], Jeremy Lim[4], Tao Liu[16,17], Ashish K. Meena[12], Jose M. Palencia[5], George F. Smoot[1,18,19,20], and Liliya L.R. Williams[6]
[1] Donostia International Physics Center, DIPC, Basque Country, San Sebastián, 20018, Spain; tom.j.broadhurst@gmail.com
[2] Department of Physics, University of Basque Country UPV/EHU, Bilbao, Spain
[3] Ikerbasque, Basque Foundation for Science, Bilbao, Spain
[4] Department of Physics, The University of Hong Kong, Pokfulam Road, Hong Kong
[5] IFCA, Instituto de Física de Cantabria (UC-CSIC), Av. de Los Castros s/n, 39005 Santander, Spain
[6] Minnesota Institute for Astrophysics, University of Minnesota, 116 Church St. SE, Minneapolis, MN 55455, USA
[7] Center for Astrophysics | Harvard & Smithsonian, 60 Garden St., Cambridge, MA 02138, USA
[8] Steward Observatory, University of Arizona, 933 N. Cherry Ave., Tucson, AZ 85721, USA
[9] Center for Frontier Science, Chiba University, 1-33 Yayoi-cho, Inage-ku, Chiba 263-8522, Japan
[10] Department of Physics, Graduate School of Science, Chiba University, Chiba 263-8522, Japan
[11] School of Earth and Space Exploration, Arizona State University, Tempe, AZ 85287-1404, USA
[12] Department of Physics, Ben-Gurion University of the Negev, PO Box 653, Be'er-Sheva 8410501, Israel
[13] Department of Physics, Oklahoma State University, 145 Physical Sciences Bldg., Stillwater, OK 74078, USA
[14] Department of Physics, University of California, 366 Physics North MC 7300, Berkeley, CA 94720, USA
[15] Department of Physics, School of Science, The University of Tokyo, Bunkyo, Tokyo 113-0033, Japan
[16] Department of Physics, The Hong Kong University of Science and Technology, Hong Kong S.A.R., People's Republic of China
[17] Jockey Club Institute for Advanced Study, The Hong Kong University of Science and Technology, Hong Kong S.A.R., People's Republic of China
[18] Department of Physics and Institute for Advanced Study, The Hong Kong University of Science and Technology, Hong Kong
[19] Paris Centre for Cosmological Physics, APC, AstroParticule et Cosmologie, Université de Paris, CNRS/IN2P3, CEA/lrfu, 10, rue Alice Domon et Leonie Duquet, 75205 Paris CEDEX 13, France
[20] Physics Department, University of California at Berkeley, CA 94720, USA
Received 2024 June 13; revised 2024 November 25; accepted 2024 November 25; published 2024 December 23

Abstract

Many microlensed stars discovered by JWST closely follow the winding critical curve of A370 along the "Dragon Arc" with $m_{AB} > 26.5$, which we show comprises asymptotic giant branch stars microlensed by the observed level of diffuse cluster stars, corresponding to $\simeq$1% of the dark matter density. Most events appear along the inner edge of the critical curve, following an asymmetric band of width $\simeq$4.5 kpc that is skewed by -0.7 ± 0.2 kpc. This asymmetry, we argue, follows from the parity difference in caustic structure inherent to microlensing that extends to higher magnification in the negative parity regions. This parity difference predicts a modest net shift of -0.04 kpc to the inside of the cluster critical curve within a narrower band of $\simeq$1.4 kpc than observed. Adding cold-dark-matter-like subhalos of $10^{6-8}\,M_{\odot}$ doubles the width, but detections are predicted to favor the outside of the critical curve, where the subhalos generate local Einstein rings, and subhalos inside the critical curve depress the magnification, reducing microlensing. Instead, the density perturbations of "wave dark matter" as a Bose–Einstein condensate (ψDM) can generate a wide band of corrugated critical curves with a large negative asymmetry. We find that a de Broglie wavelength of $\simeq$10 pc reproduces the observed width of 4.5 kpc, with a negative skewness $\simeq -0.6$ kpc, like the data, corresponding to a boson mass of $\simeq 10^{-22}$ eV, in agreement with dwarf galaxy dynamical estimates. Independently, we also find clear asymmetry in the Jupiter Arc, with 12 microlensed stars lying along the inside of the critical curve, like the Dragon Arc.

Unified Astronomy Thesaurus concepts: Gravitational lensing (670)

1. Introduction

Detection of microlensed stars at cosmological distances has become routine in cadenced JWST imaging (P. L. Kelly et al. 2023). These are typically found where lensed galaxies are bisected by the radial or tangential critical curves of massive lensing clusters. The host galaxies showing microlensing are preferentially of modest redshift, which is to be expected given the rapidly increasing luminosity distance with redshift, so that in practice, supergiant stars become much harder to detect at $z > 2$. These microlensed stars are recognized by flux variation, including clear cases of caustic crossing where the magnification saturates for some hours as the caustic crosses the finite area stellar disk and then suddenly disappears on the other side of the caustic. The first example at cosmological distances, "Icarus," was discovered serendipitously (P. L. Kelly et al. 2018), with other cases subsequently discovered (S. A. Rodney et al. 2018; W. Chen et al. 2019), as originally anticipated for hugely magnified blue giants (J. Miralda-Escude 1991) when the star is crossed by the critical curve of a massive lens in relative motion. It has now become clear that microlensing is affecting these light curves, and this should not be surprising, as even the relatively modest projected mass density of diffuse cluster stars observed as intracluster light (ICL) is sufficient to account for the observed light-curve variation, with a projected stellar surface mass density of typically 10 $M_{\odot}\,\mathrm{pc}^{-2}$,

representing only 1% of the total projected column of matter at the location of stars on the Einstein radius, where dark matter dominates (T. Venumadhav et al. 2017; J. M. Diego et al. 2018). This consistency with the observed surface brightness of the ICL severely restricts any additional nonstellar microlensing mass, for example, LIGO-like black holes, for which frequent, low-amplitude brightness fluctuations should be seen, unlike the data (J. M. Diego et al. 2018; C. Vall Müller & J. Miralda-Escudé 2024).

Related to these transients, we have also recognized a puzzling class of "one-sided" unresolved sources, noticeably offset from the cluster critical curves by up to a few kiloparsecs (J. M. Diego et al. 2023; A. K. Meena et al. 2023a), with a conspicuous absence of the predicted counterimage on the other side of the cluster critical curve. This absence may be blamed on microlensing by ICL stars in the cluster, millilensing by a dark perturbing halo, or unseen, dim globular clusters. One of these transients detected as part of the Hubble "Flashlights" program (P. L. Kelly et al. 2022) near the center of an arc behind A370 at $z = 1.27$ (unrelated to the Dragon Arc) has a puzzlingly large offset of 3 kpc ($\sim 0\farcs5$) from the tangential critical curve of A370 (A. K. Meena et al. 2023b). We note that this transient appears "inside" the critical curve of the cluster A370 with negative image parity, as is also the case for three more microlensed transients detected recently by JWST in fold arcs behind other lensing clusters, including A2744 ($z = 2.65$; W. Chen et al. 2022), "Mothra" ($z = 2.09$; J. M. Diego et al. 2023), and "Quyllur"($z = 2.19$; J. M. Diego et al. 2023), with offsets of $\simeq 0\farcs1$ to the negative parity side of the respective tangential critical curves. Repeat imaging of the higher-redshift "one-sided" cases has not found time variation, disfavoring microlensing and pointing to unresolved star clusters that may be "millilensed" by dark perturbations (L. Dai et al. 2018, 2020; J. M. Diego et al. 2024). Millilensing, unlike microlensing, has a relatively low density of critical curves, so high-magnification caustic crossing is unlikely and thus insufficient for detection of a distant star. Instead, such cases may be compact, luminous star clusters of modest magnification, sufficient for detection but not enough to be resolved and too far from the critical curve to cause large time variation (L. Dai 2021). Thus, millilensed star clusters may provide a more plausible explanation for the higher-redshift, unresolved, persistent "one-sided" cases so that excessive microlensing magnification need not be invoked, such as "Earendel" ($z = 6.2$; B. Welch et al. 2022) or "Godzilla" (J. M. Diego et al. 2022; $z = 2.4$), for which a dense, young star cluster explanation is preferred spectroscopically (M. Pascale & L. Dai 2024), and plausibly also for "MACS0647-star-1" ($z = 4.8$; L. J. Furtak et al. 2024). The millilensing scale corresponds to subhalos of 10^{6-8} $M_\odot$, and the absence of detected starlight, even in deep JWST images, excludes normal globular clusters, preferring dark matter possibilities such as dark, low-mass cold dark matter (CDM) halos or the pervasive lensing corrugations of wave dark matter, ψDM, as a Bose–Einstein condensate (J. H. H. Chan et al. 2020; H. Kawai et al. 2022; A. Amruth et al. 2023). Further modeling of millilensing substructure is needed to evaluate whether flux anomalies are sufficient to account for such one-sided detections of star clusters. Here we will explore the combination of millilensing induced by dark matter substructure, together with the level of microlensing by stars comprising the diffuse ICL.

Substructure is predicted for CDM as unseen halos below the visible galaxy scale of about $<10^8$ $M_\odot$, and pervasive substructure is predicted for wave dark matter ψDM by de Broglie scale-wave interference as a Bose–Einstein condensate, where the boson mass, m_ψ, is the only free parameter. These fluctuations are equally positive and negative as they range over constructive to destructive interference with full density modulation on the de Broglie scale, $\lambda_{\rm dB}$ (H.-Y. Schive et al. 2014). In contrast, warm dark matter will be smoothed by early free streaming depending on the associated particle mass, estimated to be in the keV range. However, lensing data have indicated that invisible substructure is common with "flux anomalies" typical of multiply lensed QSOs, differing by $\simeq$30% relative to smooth lens models (A. M. Nierenberg et al. 2020) but consistent with the level of local flux anomaly predicted for ψDM (A. Amruth et al. 2023). Furthermore, milliarcsecond-scale "positional anomalies" are now recognized in high-resolution radio images of compact sources lensed by individual massive galaxies (P. Hartley et al. 2019). These lensing anomalies may also imply a population of dark CDM subhalo perturbations, if not erased over time by tidal forces, as small perturbing Einstein rings should be seen along the outer edge of the critical curve for CDM-like subhalos (L. L. R. Williams et al. 2023; K. T. Abe et al. 2024), whereas for ψDM, the perturbations are like a Gaussian random field (GRF; T. Venumadhav et al. 2017; A. Amruth et al. 2023).

A new opportunity to examine dark matter substructure is provided by the large set of over 40 microlensed stars reported by Y. Fudamoto et al. (2024) within the original "Dragon Arc," the first known giant arc, a relatively low-redshift, $z = 0.735$, bright spiral galaxy lensed by the massive cluster A370 ($z = 0.37$). These transients add to the 10 blue giants recently detected by Hubble in the Dragon Arc as part of the Flashlights program (P. L. Kelly et al. 2022; S. K. Li et al. 2024). This new discovery of abundant microlensed stars in the Dragon Arc allows direct tests for dark matter substructure (L. Dai 2021; J. M. Diego et al. 2024) complementing millilensing methods (J. Wagner 2019; A. Amruth et al. 2023). In Section 1, we first model the observed number counts of events to identify the stellar class responsible for the majority of JWST events and their magnification by combining statistical microlensing with stellar synthesis code calculations, following the pioneering JWST predictions for microlensing at cosmological distances (R. A. Windhorst et al. 2018; A. K. Meena et al. 2022). In Section 2, we explore the simplest case of smooth dark matter for the cluster with the observed level of microlensing implied by the diffuse ICL measured adjacent to the Dragon Arc. In Section 3, we add CDM subhalos, and we also explore ψDM with our perturbation-generating code for comparison with the width of the microlensing band and its asymmetry. Note that at the redshift of the lensing cluster A370, $z = 0.37$, 1" corresponds to a scale of 5.2 kpc in the lens plane for standard cosmology.

2. Origin of Microlensed Stars in the Dragon Arc

We first examine the brightness distribution of the microlensed events detected by JWST, as recently reported by Y. Fudamoto et al. (2024), found with NIRCam imaging, first Cycle 1 GTO-1208 (the CAnadian NIRISS Unbiased Cluster Survey; PI: C. Willot) and then Cycle 2 GO-3538 (PI: E. Iani) targeting A370 ($z = 0.375$) using multiple NIRCam filters, separated by ~1 yr. The number counts of these detections are

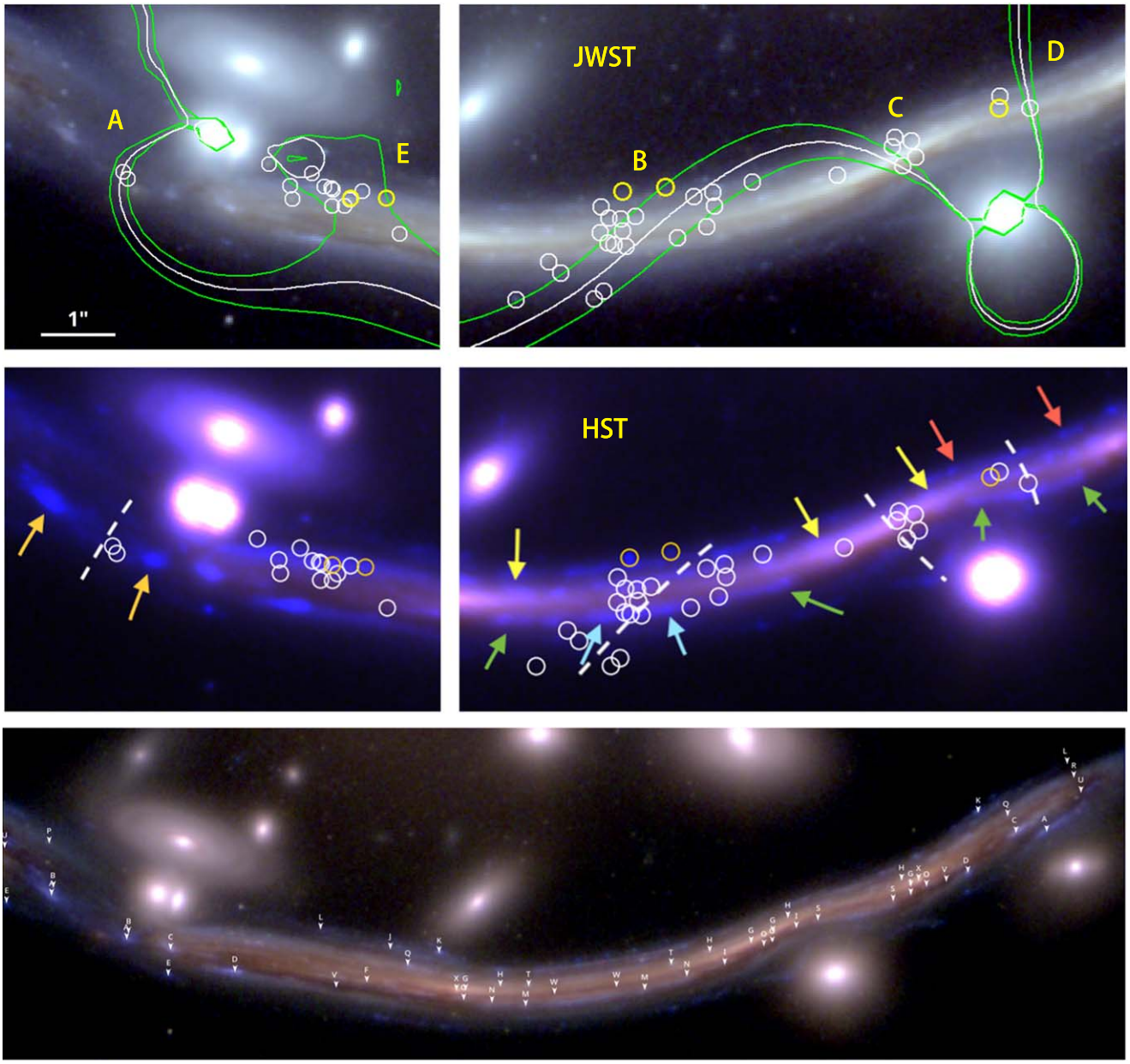

Figure 1. The top panel shown the JWST transients found in the Dragon Arc (Y. Fudamoto et al. 2024), shown as white circles, plus those found by our Flashlights/Hubble program (P. L. Kelly et al. 2022), shown as yellow circles, revealing that the microlenses closely follow the critical curve, appearing along all four intersections of the Dragon Arc with the tangential critical curve, labeled A, B, C, and D, implying that these events are highly magnified. The tangential critical curve in the upper panels is indicated by the white line and bracketed by green lines showing the $\mu = \pm 100$ magnification contours from the free-form strong-lensing WSLAP+ code (J. M. Diego et al. 2024) using over 90 multiply lensed galaxies and made independently, prior to the discovery of microlensing here. The right-hand panel shows the accuracy of the critical curve at the A and B intersections, where it agrees precisely with the symmetry of internal features identified in Hubble and JWST. The middle panel shows the deep Hubble images from our Flashlights program showing many internal pairs of features, some of which are marked with arrows here and color coded to indicate where reflection symmetry pins down the path of the winding critical curve of A370 as it crosses the Dragon Arc. This also demonstrates the good agreement of this model-independent critical path with the WSLAP+ model shown in the top panel. The bottom panel shows the multiple imaged features now identified in the Dragon Arc, including our recent deep Flashlights imaging program, resulting in a model precision of $<0.''05$ in defining the path of the critical curves when using our WSLAP+ flexible strong-lensing method (shown in the top panel). A table of these new multiply lensed knots is available upon request for independent lens modeling.

plotted in Figure 1. We model these data with an established stellar synthesis code with a star formation history appropriate for the lensed disk galaxy, aka the Dragon Arc, using the Stellar Population Interface for Stellar Evolution and Atmospheres (M. W. J. Hosek et al. 2020) to trace the stellar evolution based on a star formation history suited to the spiral galaxy that is lensed into the Dragon Arc, given its redshift and optical-IR photometry. This star formation history is estimated through SED fitting with BAGPIPES (A. C. Carnall et al. 2018) with a Kroupa initial mass function (IMF; P. Kroupa 2001). A more detailed discussion of the methodology, including the effect of the choice of different model parameters, can be found in S. K. Li et. al. (2024, in preparation). The observations can be accessed via 10.17909/c9k4-c592 from the Mikulski

Archive for Space Telescopes at the Space Telescope Science Institute.

The model-generated stellar population generated at any given time step is then input into our microlensing calculations with a predefined set of probability distribution functions (PDFs) calculated numerically as a function of both the stellar surface density in the lens and the level of macromagnification of the lensing host of the microlenses, as outlined in J. M. Palencia et al. (2023). It is notable that even the modest, commonly observed percent levels of projected stellar mass compared to the total column of dark matter near the Einstein radius of a cluster, $\kappa_\star \simeq 0.01$, can generate trails of multiply microlensed star images that appear and disappear on a wide range of timescales in the optically thick microlensing region close to a cluster critical curve (J. M. Diego et al. 2018).

The ICL starlight at the location of the Dragon Arc translates to a surface mass density of about $18\,M_\odot\,\mathrm{pc}^{-2}$ for the Kroupa IMF, or about 1% of the total column of dark matter near the Dragon Arc. With this, we can generate statistical distributions of microlensed stars for comparison with the observed JWST transients in the F200W band, $m_{AB} < 28.6$. We can now predict the number counts, $N_L(<m)$, of microlensed events as a function of lens magnification relative to the unlensed counts at fixed apparent magnitude, $N_o(<m)$. Predictions for the microlensing rate must include this magnification bias (T. J. Broadhurst et al. 1995),

$$N_L(<m)/N_o(<m) = \mu^{2.5\gamma(m)-1}, \quad (1)$$

showing the competition between the reduced source plane area, μ^{-1}, and enhanced magnified depth at the apparent magnitude, $m + 2.5\log\mu$, leading to a net enhancement in numbers, or positive magnification bias, when the slope of the counts is steeper than the break-even value, $\gamma(m) = d\log N(<m)/dm > 0.4$. This magnification bias is sizable for the steep bright end of the observed counts, $\gamma \simeq 0.7$, as shown in Figure 2, where we compare our predictions with the Dragon Arc.

We see that the steep counts are well matched by our normalized predictions in Figure 2, where the solid black curve in Figure 2 represents the combined negative and positive parity images, for which we also show that there is a small asymmetry, which is small in relation to the count slope but as we show later does significantly differ across the cluster critical curve, shown in Figure 2. For these predicted detections the mean magnification of the microlens and background cluster magnification is close to $\mu \simeq 10^3$ and corresponds to luminous red giants in the Dragon Arc, with absolute magnitudes of $-8 < M_{AB} < -6$, in the F200W band of JWST.

3. Smooth Dark Matter plus Stellar Microlenses

The simplest combination of stellar microlensing added to a smooth distribution of dark matter has been explored in detail since the discovery of "Icarus," the first microlensed star at cosmological distances, a blue supergiant in the spiral arm of a lensed galaxy at $z = 1.49$ (P. L. Kelly et al. 2016) near the critical curve of the massive cluster MACS J1149+2223 ($z = 0.54$). A relatively modest projected density of stellar mass is now appreciated to be sufficient for generating the microlensing of Icarus and other transient stars near the critical curve of other lensing clusters with a projected mass density typically observed to be about 1% of the total projected mass

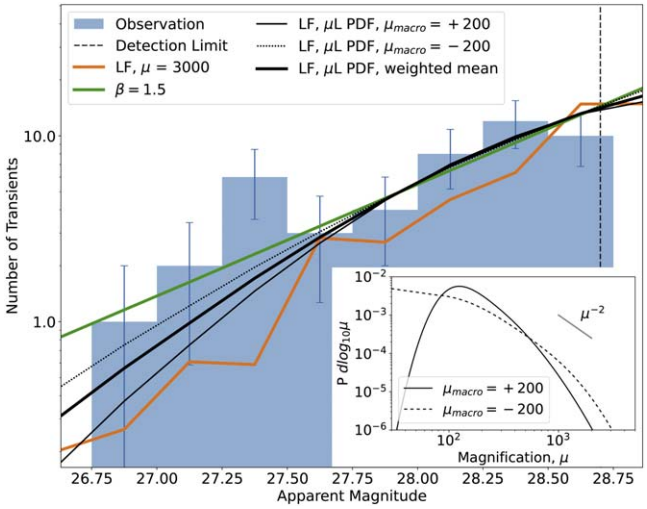

Figure 2. Microlensed events detected by JWST, with magnitudes measured in the F200W band of JWST, compared with the stellar synthesis code luminosity function (LF) predicted for an evolved spiral galaxy. The black curve includes microlensing by the stars comprising the diffuse cluster light. This accounts well for the brightness distribution of microlensed stars above the flux limit (vertical black line) and corresponds to red giant AGB stars. The orange curve shows the unlensed stellar LF simply shifted by a mean magnification, $\mu = 3000$ or 7.5 mag, approximately matching the data. The green line is a power-law fit to the count slope of $\beta = 1.5$, well above the lensing invariant slope ($\beta = 1.0$); i.e., a positive magnification bias is expected, and thus a larger number of microlensing events is potentially accessible in modestly deeper images of the Dragon Arc. These calculations account for the parity dependence of the magnification distribution shown in the inset, in particular the longer tail to higher magnification that allows lower-luminosity stars to be detected. The curves in the inset are for the choice of a mean "macro-magnification" of $\mu = \pm 200$ near the mean magnification that "underlies" the microlensing predicted for their observed locations relative to the cluster critical curve, as seen in Figure 1.

density at the Einstein radius of the cluster, where the scale of microlensing is effectively magnified by the macrolensing of the cluster to become the main source of magnification.

Numerical calculations show that the critical curves of the microlensing stars are effectively magnified by the tangential magnification factor μ_t, becoming a dense web at high optical depth, $\tau > 1$, where $\mu_t\kappa_\star > 1$. In practice, this transition occurs with a typical stellar density of microlenses $\kappa_* = 0.01$, corresponding to $\mu > 100$, near the Einstein radius. Most of the observed lensed events fall within this range, $|\mu| > 100$, delineated in green in Figure 1, spanning a band of $\simeq$4 kpc about the predicted critical curve of A370. The ideal critical curve for a smooth cluster lensing profile is replaced by a dense corrugated band of critical curves centered on the cluster critical radius. Then the peak magnification of background stars occurs when any microlensing caustic sweeps past the observer, with a transverse peculiar velocity dominated by the lensing cluster ($\simeq$1000 km s^{-1}) that highly magnifies small background sources. The peak magnification of a star of finite radius is set by the density of the microlensing network, i.e., by the optical depth of microlensing, τ, which is proportional to the product of $\mu_t\Sigma_\star$. This generates peak levels of microlensing as the microlensing caustic network crosses the lensed stars reaching $\mu_{\max} \simeq 10^{3-4}$ for $\kappa_\star \simeq 0.01$ lasting hours to days depending on the star radius and relative transverse velocity, v_t, simply $t_{\rm peak} = 2R_\star/v_t$, and this will be repeated for a given star on average every few years (T. Venumadhav et al. 2017; J. M. Diego et al. 2018; M. Oguri et al. 2018; L. Weisenbach et al. 2024).

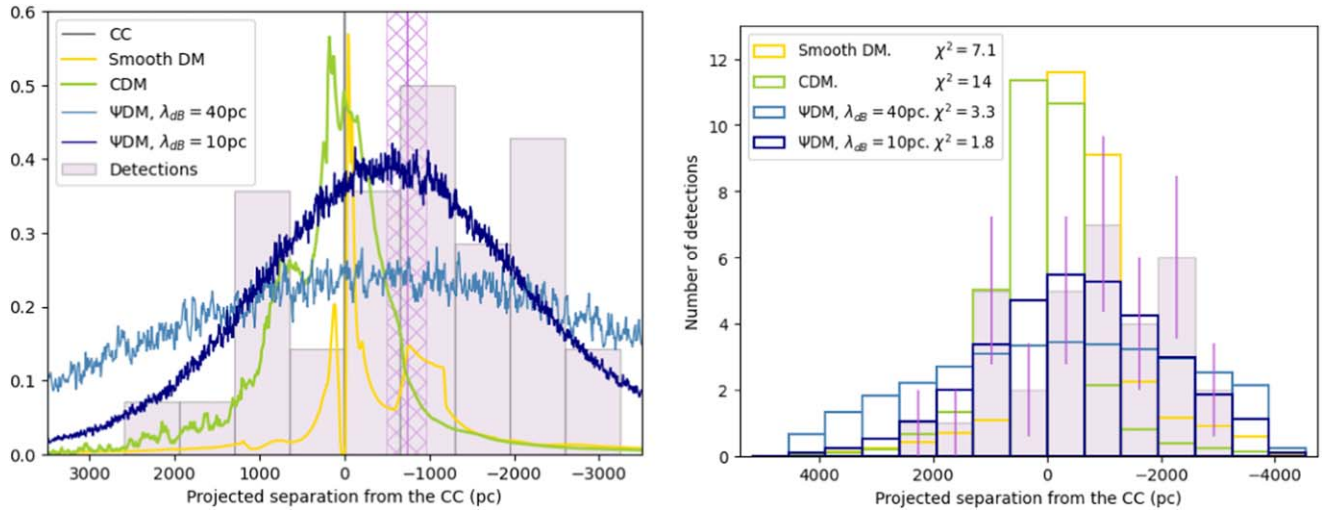

Figure 3. The offset distribution of JWST transients (33 detections) along all four intersections of the Dragon Arc traversed by the tangential critical curve of A370, labeled A, B, C, and D in Figure 1. The left panel shows the form of the predicted distributions for comparison with the asymmetric distribution of the data, which favors negative offsets interior to the cluster critical curve, with a mean of -0.7 ± 0.2 kpc shown by the hatched vertical band. The broad spread with negative skewness of the observed histogram best resembles ψDM, with a de Broglie scale of 10 pc favored with $\chi_r^2 = 1.8$, as shown on the right, compared to ψDM with a larger de Broglie scale of 40 pc. The data are in significant tension with the centrally peaked smooth dark matter model shown in yellow and the CDM-based subhalo model shown in green, as detections are skewed positive, unlike the data.

Ray tracing at high resolution has uncovered an important difference in the distribution of microlensing magnification due to the switch in the sign of the local orthogonal stretch factors, from $1 - \kappa + \gamma$ to $1 - \kappa - \gamma$ at the Einstein radius, which causes the radially directed "figure-eight-shaped" critical curve of a point mass on the outside to be tangentially aligned with the critical curve on the inside and more magnified by the boost in magnification parallel to the cluster curve (T. Venumadhav et al. 2017; J. M. Diego et al. 2018). Recent high-resolution simulations described above (J. M. Palencia et al. 2023) have now provided more detailed predictions for the distribution of magnifications as a function of the underlying macromagnification and the projected surface mass density of microlensing stars. This parity dependence is shown in the inset in Figure 2 and allows a reliable comparison with the observations for the high optical depth regime $\tau > 1$, where numerical predictions are essential and have demonstrated an important distinction between the image parity regimes inside and outside the critical curve, where a longer tail to high negative magnifications is predicted for microlensing with $\tau > 1$ leading to a higher detection rate on the inside of the cluster critical curve, as we emphasize here and shown in the inset of Figure 2. At the highest magnifications, the predicted distribution turns over more steeply than μ^{-2} (Figure 2), as caustics cross at high optical depth for microlensing, becoming lognormal when $\tau > 1$, such that the lower the stellar surface density of the microlenses, the higher the magnifications reached; see L. Weisenbach et al. (2024), Equation (17). We use the set of PDFs determined by J. M. Palencia et al. (2023) as a function of microlensing stellar mass density and the underlying "smooth" magnification tabulated by J. M. Palencia et al. (2023), and our source population of asymptotic giant branch (AGB)/red giant branch (RGB) stars is as described in the previous section when modeling the number counts of the lensed detections. The result is a predicted distribution of detections that is sharply peaked along the critical curve of the macrolens, shown in Figure 3, and a predicted width of the band of detectable images of 1.4 kpc, shown in in predicted width of the band of detectable images is 1.4 kpc, corresponding to the estimated surface density of microlensing stars in the cluster given by the observed level of ICL for the Dragon Arc (A. K. Meena et al. 2023) of $\simeq 18\, M_\odot\, \mathrm{pc}^{-2}$. This prediction is significantly narrower than the observed spread of 4.5 kpc measured in the data (Figure 3). We also predict a modest asymmetry in the distribution of detections toward negative parity of about -0.04 kpc to the inside of the critical curve in the direction of the cluster center, due to the parity effect, and this is also significantly smaller than the observed shift of -0.7 ± 0.2 kpc, shown in Figure 3. The "smooth" model considered here can be regarded as warm dark matter, where halo formation is taken to be strongly suppressed by free streaming, below the milliarcsecond scale of visible galaxies. We now go on to explore substructure in the dark matter, as is well motivated by many galaxy- and cluster-scale observations of image flux and positional anomalies that are well known to affect compact highly magnified sources that are understood to have a significant effect on the width of the band of detectable microlenses by inducing millilensing corrugations that modulate the detection of microlenses, as described below.

4. Adding Dark CDM Subhalos

The breadth of the microlensing region can be increased by a population of dark halos, as explored by L. L. R. Williams et al. (2023) in the context of the Flashlights program, showing that there is a distinct preference for new critical curves to form around halos that lie outside of the critical curve (see also K. T. Abe et al. 2024). We follow this prescription including a power-law distribution of subhalo masses with $dN/d\log m_{\rm halo} \propto m_{\rm halo}^{-0.9}$ in the relevant mass range $10^{6-8}\, M_\odot$ (L. Dai et al. 2018, 2020), for which we adopt concentrated Navarro–Frenk–White (NFW) profiles for these dark halos, with $C_{\rm NFW} = 30$ appropriate for their relatively low masses (J. F. Navarro et al. 1997). We see in Figure 3 that such a population of dark halo CDM can be chosen to broaden the critical region as desired by several kiloparsecs but with a clear preference for the new critical curves to appear outside the

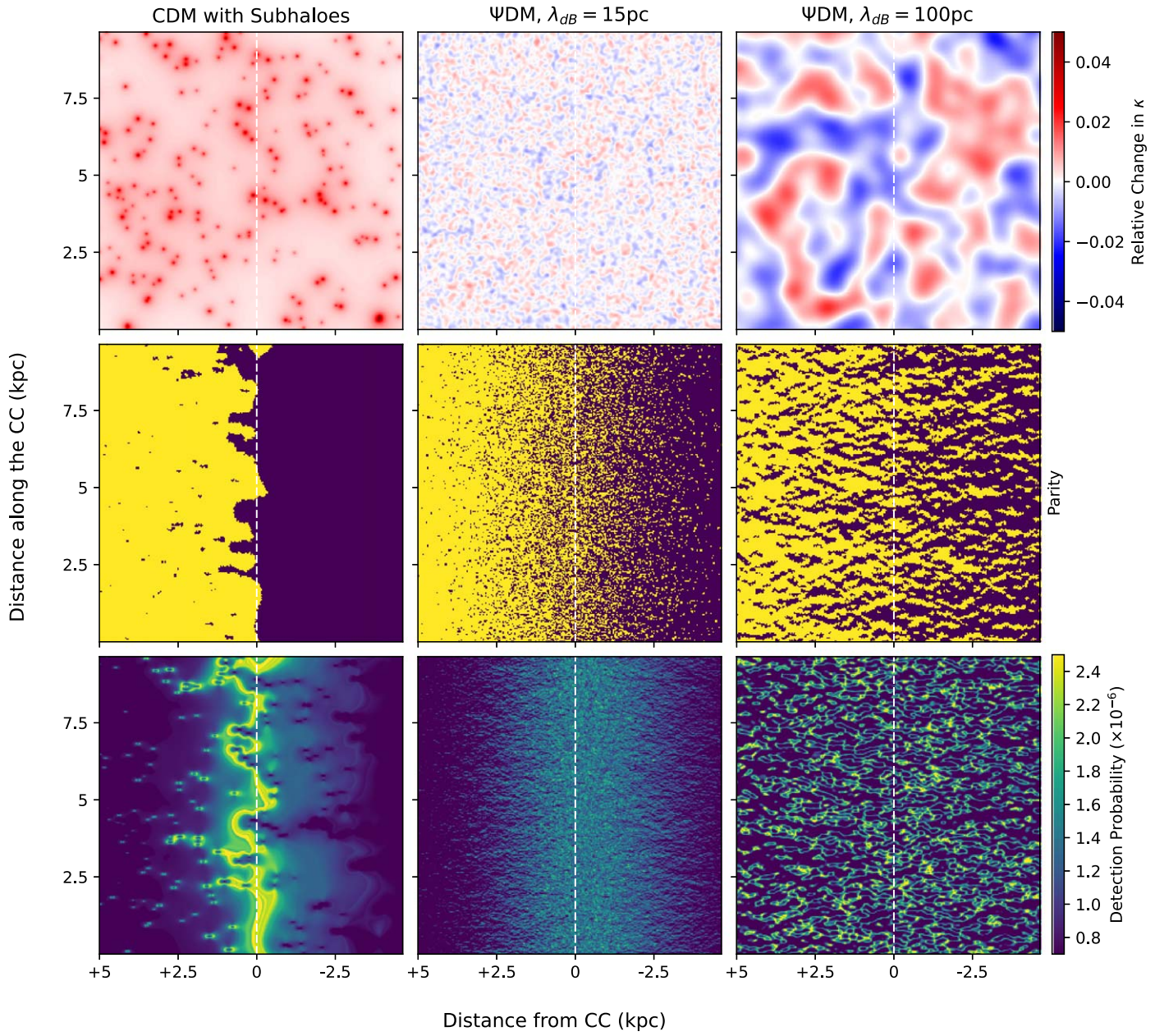

Figure 4. Lensing substructure predictions. The top row shows the substructure perturbations for CDM for subhalos of $10^{6-8}\,M_{\odot}$ (top left) and for ψDM for two choices of de Broglie wavelength, 15 pc and 100 pc (top center and top right, respectively, and zoomed in by a factor of 6 so the de Broglie wave structure is visible). The horizontal distance axis has an origin at the critical curve, with negative distance corresponding to the interior of the critical curve, marked by the dashed line, and the vertical axis is simply relative distance. The middle row shows the corresponding map of image parity (yellow for positive and purple for negative parity), showing the fingers of negative parity and locally around subhalos in the region outside the cluster critical curve and unlike the symmetric pattern for ψDM, where parity is seen to become smoothly more negative toward the cluster center on the right, with critical curves that follow all the parity transition boundaries. The bottom row shows the corresponding microlensing detection probability, calculated by including the parity-dependent microlensing magnification probability distribution, convolved with the lensed AGB/RGB stellar luminosity function and with the detection limit of JWST imposed. It can be seen that the microlensing detections are predicted to trace these critical curves, but notice how the subhalos of CDM act to locally depress the magnification interior to the critical curve, with a clear absence of associated critical curves and hence reduced interior microlensing. For ψDM, a broad network of critical curves can be seen to form, which, for $\lambda_{\rm dB} = 15$ pc, ranges over a $\simeq$4 kpc band (top center), like the data. A much larger spread is predicted for $\lambda_{\psi} = 100$ pc de Broglie (top right), spread over $\simeq$40 kpc, much broader than the observations. The band of detections is seen to be shifted to the inside of the cluster critical line for ψDM by about -0.6 kpc for $\lambda_{\psi} = 15$ pc (center bottom), like the data, caused by the longer tail to higher magnification for negative parity images.

critical radius of the cluster, where the excess subhalo mass can exceed the critical density for lensing and thereby generate local Einstein rings around the subhalos located there. The opposite behavior is predicted on the inside of the critical curve, as the critical density is already exceeded, and instead, locally reduced magnification is predicted for each subhalo and thus local critical curves are not generated, as can be seen in Figure 4. Also shown in Figure 4 is the addition of microlensing described by the magnification-dependent probability densities described in Section 1 for the high optical depth τ regime, with the detection limit of $m_{AB} = 28.3$ set by the JWST observations of the Dragon Arc. This is shown in the bottom left panel of Figure 4, where it can be seen that the critical curves remain visible above a smoother background of

transients, thus skewing detectable microlensing to the outside of the cluster critical curve, unlike the data where the opposite tendency is apparent.

5. Wave Dark Matter

The above disagreement in terms of skewness for CDM-like dark halos motivates us to consider wave/fuzzy dark matter, ψDM, as a simple, desirable proposal for the dark matter (H.-Y. Schive et al. 2014; L. Hui et al. 2017; J. C. Niemeyer 2020; L. Hui 2021) given the now stringent absence of weakly interacting massive particles and the natural solution that ψDM provides for the small-scale problems of CDM, with its inherent Jeans scale (H.-Y. Schive et al. 2014; J. C. Niemeyer 2020). Simulations in this context have revealed a surprisingly rich wave structure due to interference, including a central soliton that is widest at low momentum, providing a natural explanation for the large cores of common dwarf spheroidal (dSph) galaxies (H.-Y. Schive et al. 2014; A. Pozo et al. 2024). Unique lensing effects are also to be expected, due to the full density modulation of the ψDM in cluster halos that leads to a wide corrugated band of critical curves all along the Einstein radius of a lensing galaxy or cluster at a level that depends on the projection of independent de Broglie–scale fluctuations along the line of sight, resulting in a GRF of perturbations, by the central limit theorem. The surface density at a projected radius R, $\Sigma(R)$, is perturbed by $\Delta\Sigma(R_h)/\Sigma(R_h) \simeq (\lambda_{dB}/R_h)^{0.5}$, where R_h is the effective halo size at the Einstein radius (T. Venumadhav et al. 2017; H. Kawai et al. 2022; L. Weisenbach et al. 2024). This corresponds to a 1% dispersion relative to the mean surface mass density at the Einstein radius of the massive cluster, where $R \simeq 100$ kpc and a de Broglie scale of $\lambda \simeq 10$ pc is predicted (see below). Interestingly, this says that the perturbation amplitude increases toward the cluster center, as there are fewer independent cells of $\lambda_{\rm dB}$ relative to the projected radius, R; hence, larger-density perturbations of 2%–3% are expected near the radial critical curve with strong lensing effects.

For clusters, the de Broglie wavelength should be relatively small, scaling with the widely adopted core–halo scaling relation (H.-Y. Schive et al. 2014)

$$\lambda_{\rm dB} = 15 \left(\frac{10^{-22}\ {\rm eV}}{m_\psi}\right)\left(\frac{10^{15}\,M_\odot}{M_{\rm halo}}\right)^{1/3}\ {\rm pc}\ , \qquad (2)$$

where m_ψ is the boson mass of ψDM. For masses $m_\psi \approx 10^{-22}$ eV and a $10^{15}\,M_\odot$ cluster, this corresponds to 3 mas in the lens plane. This core–halo relation is not established at high halo mass, as simulations of ψDM do not yet have sufficient resolution to resolve the small de Broglie wavelength appropriate for galaxy clusters, but the uncertainly principle provides a simpler scaling using velocity dispersion, which for dSph galaxies is typically $\simeq$10 km s^{-1} and for massive clusters is $\simeq$1000 km s^{-1}, so $\lambda_{\rm clus}/\lambda_{\rm dSph} = (\sigma_{\rm clus}/\sigma_{\rm dSph})^{-1} = 0.01$; i.e., we simply expect $\lambda_{\rm clus} \simeq 10$ pc. We can also predict the width of the corrugated band, Δ_ψ, as a function of $\lambda_{\rm dB}$ and the observed Einstein radius of the cluster, $\theta_{\rm E}$, and with the GRF condition above, we have $\Delta\Sigma_E \sim \Sigma_E \sqrt{\lambda_{db}/R_h}$, and we can adopt $R_h \sim 100$ pc at the projected radius of the Dragon Arc and surface mass density at the Einstein radius, $\theta_{\rm E}$, of $0.7 \times \Sigma_{\rm crit}$ for the cluster NFW profile:

$$\Delta\theta_\psi \simeq \theta_{\rm E} \times 0.0022\sqrt{\lambda_{\rm db}/1\ {\rm pc}}\,. \qquad (3)$$

For $\lambda_{\rm dB} = 15$ pc and an Einstein radius of approximately 30″ for A370 at the redshift of the Dragon Arc, this predicts a full width of $2\Delta\theta_\psi = 0.''52$ or 3.8 kpc, which we see in Figure 3 is indeed close to the observed width. In addition to this band of critical curves, we add the microlensing from starlight in the ICL visible at the location of the Dragon Arc, described above with 18 $M_\odot$ pc^{-2} (A. K. Meena et al. 2023) or about 1% of the dominant dark matter column at the Dragon Arc location. The top row of Figure 4 shows the magnification pattern for two choices of boson mass, including the prior predicted 10 pc scale based on local dSph dwarf galaxy cores and a larger 100 pc scale, where more detail of the corrugated pattern is visible. As can be seen in Figure 4, the width of the magnified band of critical curves is about 4 kpc for $\lambda_{\rm dB} = 10$ pc, similar to the data, but it would be 40 kpc, 1 order of magnitude larger, for $\lambda_{\rm dB} = 100$ pc, scaling as $\propto\sqrt{\lambda_{\rm dB}}$ and completely excluded by the data.

The effect of microlensing is to bias the detections to smaller radii, inside the critical curve of the cluster, at a level of about −0.53 kpc for $\lambda_{\rm dB} = 10$ pc, as seen in the bottom central panel of Figure 4, and similar to the observed offset of -0.7 ± 0.2 kpc for the data, indicated in Figure 3. This asymmetry in the microlensing band relative the symmetric band of the critical curves follows from the higher magnification for negative parity images and the positive magnification bias for red giant stars (see Figure 2). We also show the major qualitative difference between CDM and ψDM in Figure 5 to illustrate the origin of this shift in terms of parity. The positive density peaks for CDM-like subhalos only generate new critical curves beyond the Einstein radius of the cluster, whereas

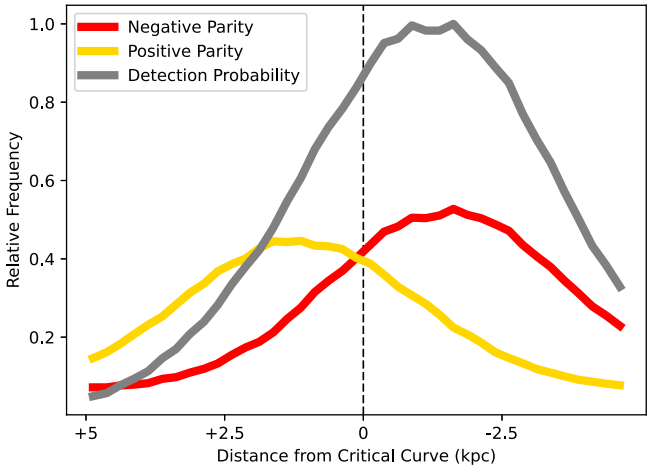

Figure 5. The effect of parity on the detection of microlensing caused by ψDM, with a de Broglie scale set to 15 pc. The yellow curve indicates the proportion of the image plane area with high magnification $\mu > 100$, which peaks to the outside of the critical curve, corresponding to the yellow area of the 2D parity map shown in Figure 4, following the broad network of corrugated critical curves. The red curve shows the same for negative parity, i.e., where $\mu < -100$, following the same broad network of critical curves shown in Figure 4. The yellow and red curves are almost mirror symmetric, but a significant asymmetry arises from the inherent geometric distinction between positive and negative microlensing caustics, resulting in a longer tail to higher magnification for microlensed stars in the negative parity areas, as shown in the inset of Figure 1. This longer tail translates to a higher proportion of stars detectable inside the critical curve of the cluster, above the flux detection limit, shown by the gray curve, like the observed asymmetry reported here.

inside, they do not form. For ψDM the density perturbations are both positive and negative in equal numbers, generating long corrugated critical curves along the boundaries between the positive and negative parity regions shown in yellow and purple, respectively, in Figure 5. This means that the detection rate is higher in the right-hand half of this region following the larger area of negative parity along the critical curves within the Einstein radius, as can be seen in Figure 5. The exact opposite behavior is seen for the positive rim, which has more pixels around the outer side of the critical curves to the left beyond the Einstein radius of the cluster. The asymmetry then comes from the greater magnifications reached for negative parity, which enhances the detection rate in favor of the interior, thereby skewing the detection rate.

It is important to appreciate that our lensing-based boson mass agrees well with independent estimates based on soliton core fits to local dwarf galaxies that find a boson mass of $\simeq 10^{-22}$ eV, which is preferred for the dominant dark matter in the ψDM context (H.-Y. Schive et al. 2014; S.-R. Chen et al. 2017; A. Pozo et al. 2024).

6. Discussion and Conclusions

We have shown that the abundant microlensing in the Dragon Arc detected by JWST and the Hubble Space Telescope (HST) closely follows the tangential critical curve of A370. We emphasize that the path of the critical curve is accurately defined by the reflection symmetry of many internal features now recognizable within the Dragon Arc, as shown in Figure 1. Furthermore, this model-independent path is almost indistinguishable from our free-form adaptive grid-based lens model WSLAP+ (J. M. Diego et al. 2007, 2024; I. Sendra et al. 2014) built from over 90 multiply lensed galaxy images around A370 (A. Niemiec et al. 2023); also, the light-traces-mass method (A. Zitrin & T. Broadhurst 2009) can be seen to provide a reasonably good comparison with the observed distribution (Y. Fudamoto et al. 2024). Hence, we have accurately pinned down the path of the critical curve allowing a precise comparison with the microlensing events, and the tight correspondence means higher magnification is required for detection. This we estimate to have a mean level of $\mu \simeq 3000$ by convolving our stellar synthesis code with the microlensing probability distribution. We therefore disfavor interpreting these transients as very luminous giants with modest magnification, for which detections would be more uniformly spread along the Dragon Arc. Instead, most of the JWST detections we conclude correspond to AGB stars with absolute magnitudes in the range $-6 < M_{\rm F200W} < -8$, which reproduces well the observed counts that all lie faintward of F200W > 26.6, with rapidly rising numbers toward the detection limit of F200W $= 28.6$. The surprisingly large numbers of microlenses can then be understood as abundant AGB stars that are accessible due to the low redshift of the Dragon Arc ($z = 0.735$) and the depth of JWST data. It is also clear that a huge reservoir of RGB stars sits just below F200W > 28.5 that modestly deeper JWST data can access.

We have noticed an apparent asymmetry in the locations of the microlensed stars of -0.7 ± 0.2 kpc, favoring detections along the inner edge of the critical curve with a 2:1 ratio. This is very interesting, as images of negative parity are expected to reach higher magnification than on the positive parity side, reaching lower luminosity and hence more numerous stars of negative parity. We have calculated the level of skewness for the Dragon Arc by combining a stellar synthesis model with our microlensing simulations that extend to a high optical depth regime of relevance here. We predict a small negative skewness of -0.05 kpc for the combination of smooth underlying dark matter plus stellar microlensing at the observed level (given by the ICL near the Dragon Arc), which is modest compared to the skewness observed, -0.7 ± 0.2 kpc. Furthermore, microlensing should be sharply peaked in a narrow band of only 1.4 kpc, compared to the $\simeq$4 kpc wide band observed. This motivates adding invisible substructure on a larger milliarcsecond scale, such as CDM subhalos or the de Broglie scale of ψDM, to generate a wider band of critical curves that microlensing detections can follow. We have shown that CDM substructure can widen the band of microlenses significantly with subhalos in the range $10^{6-8}\ M_\odot$, as desired, but detections are predicted on average toward the outside of the critical curve, as subhalos in this region can exceed the critical density for lensing and thereby generate a local Einstein ring, whereas inside, the critical density is already exceeded, and we have found that the opposite behavior occurs, with a dip in magnification generated locally by each subhalo. Clearly, the negative skew of the Dragon Arc may then disfavor such CDM-like subhalos, and this prediction will be more stringently tested with additional cadenced JWST imaging of the Dragon Arc, now underway. Our tentative conclusion regarding CDM-like subhalos complements the upper limit on subhalos in a recent search for the source of flux anomalies for quad images of active galactic nuclei (AGN) lensed by massive galaxies in new JWST/MIRI imaging, where the absence of locally perturbing CDM-like subhalos may constrain any such population to lie below $<10^{7.3}\ M_\odot$ (A. M. Nierenberg et al. 2024).

We have emphasized that for ψDM, the relatively wide band and negative skewness of the distribution of microlenses seen in the Dragon Arc is readily accounted for by the equal levels of positive and negative density interference inherent to ψDM. This symmetry is unique to ψDM and generates critical curves that follow locally negative fluctuations interior to the Einstein radius of the cluster (A. Amruth et al. 2023), whereas outside this radius, the opposite occurs, with critical curves locally following positive fluctuations. Generally, for any clumpy dark matter, density fluctuations are only positive, including CDM, for which local critical curves are not formed for subhalos inside the Einstein radius of the cluster. We find quantitative agreement with the Dragon Arc for a de Broglie scale of about 10 pc, corresponding to $m_\psi \simeq 10^{-22}$ eV.

It is encouraging that this boson mass scale is predicted a priori from the size of local dSph galaxy cores that match the predicted central soliton ground state of ψDM, the radius of which is given by the de Broglie scale (H.-Y. Schive et al. 2014; S.-R. Chen et al. 2017; A. Pozo et al. 2024). This lensing-based result favoring ψDM reinforces recent analysis of the milliarcsecond positional "anomalies" of high-resolution radio lensing around a massive lensing galaxy, H2018+1906 (P. Hartley et al. 2019), for which a de Broglie scale of $\simeq$100 pc is favored, and this implies a boson mass of $m_\psi = 10^{-22}$ eV for the dominant dark matter when converting by the momentum scale (A. Amruth et al. 2023). Note that this momentum dependence of the de Broglie scale allows a consistency check on this scenario across mass scales, whereas for CDM, any substructure should be largely independent of mass but with some radially dependent effect from tidal forces.

Our boson mass estimate here of $\simeq 10^{-22}$ eV is consistent with the "canonical" value, which has been claimed to be significantly lighter than some independent constraints using the Lyα-forest of $>2 \times 10^{-21}$ eV (V. Iršič et al. 2017), but it should be stressed that the forest estimates are not direct and rely on analogy with warm dark matter simulations, as both have similar power spectrum suppression at high frequency (from the de Broglie scale and the free streaming scale, respectively). However, the ψDM interference introduces additional power on small scales that is pervasive, including the low-density regions probed by the Lyα-forest, where a wide range of the de Broglie scale is seen in the simulations extending to low momentum in the voids (see Figure S1 of H.-Y. Schive et al. 2014). Furthermore, the claimed discrepancy with ψDM is below line widths of $\simeq 20\,\mathrm{km\,s^{-1}}$ and only at $z > 5$ in the steeply declining Jeans turnover, where the gas temperature is degenerate with the dark matter power spectrum, and where spatial temperature variations from AGN and cluster galaxy gas heating sources (C. C. Doughty et al. 2023) add to the forest variance, with widespread metal injection and wide forest gaps (Y. Zhu et al. 2022), thus raising the observed power spectrum, but all this is too uncertain to confidently model in forest simulations. Hence, reliance on the Lyα-forest regarding the boson mass of ψDM is far less direct than our lensing-based estimate. However, insisting on more small-scale power can be simply achieved with an additional heavier boson species (K. K. Rogers & H. V. Peiris 2021), as in the generic string axiverse (A. Arvanitaki et al. 2010). An additional heaver boson is also motivated by the compact scale of the new ultrafaint galaxy class of dwarf galaxy, where a boson mass of $\simeq 2.3 \times 10^{-21}$ eV is indicated dynamically (A. Pozo et al. 2024), forming a minority of the dark matter, most of which is comprised of the canonical $\simeq 10^{-22}$ eV boson species. Galaxy formation in this two-boson model has been shown to be viable, capable of forming UFG dwarfs (H. Nhan Luu et al. 2024), and is well approximated by "mixed dark matter" models of CDM+ψDM, explored by A. Laguë et al. (2024), when limited below astrophysical scales of interest, as then the heavier boson acts approximately as CDM. We note the recent claim of a high boson mass constraint by T. Zimmermann et al. (2024) is based solely on the Leo II dwarf, but their boson mass is consistent with the Jeans-based analysis of this galaxy by others (S.-R. Chen et al. 2017; A. Pozo et al. 2024) of $1.7-3.3 \times 10^{-22}$ eV, similar to the other classical dwarfs. A lensing-based estimate of $>4.4 \times 10^{-21}$ eV is claimed by D. M. Powell et al. (2023) arguing that their reconstructed source is fully resolved with very long baseline interferometry so that sufficiently light ψDM would cause disruption. The breadth of their predicted band of ψDM critical curves is wide, about 25% of the Einstein radius, whereas a factor of 3 narrower band is predicted by Equation (3) and by comparable lens simulations of ψDM (J. H. H. Chan et al. 2020; A. Amruth et al. 2023), which would leave the source unscathed and hence insensitive to the lighter boson mass we estimate here.

We now list the main caveats that we remain most concerned about in terms of model uncertainties affecting our interpretation, together with suggestions for addressing these with additional data and modeling.

1. The predicted giant branch used as input for our microlensing predictions is expected to vary spatially given the observed color variation within the Dragon, implying that variation of the luminosity function of the giant branch stars should be modeled. Multiple giant branches are generated for nonsmooth star formation histories, and some spatial variations are already clear within the Dragon Arc, as the detection rate appears to show some variation along the critical curve. At any location in the arc, our predictions for the level of asymmetry depend sensitively on the slope of the stellar luminosity function at the bright end and, more generally, its form at lower luminosity. The steeper this bright end slope, the larger the magnification bias, given approximately by Equation (1). For ψDM, this uncertainty in slope and giant branch structure may translate into significant variations in the predicted amplitude of the asymmetry, necessitating more detailed stellar synthesis modeling that we aim to tackle as these spatial variations in microlensing rate become better defined along the critical curve with more survey detections.
2. There is uncertainty in making predictions related to the angular size of the largest giants known to extend up to 1700 $R_\odot$ when microlensed at the highest magnifications exceeding $\simeq$10,000, given the nanoarcsecond resolution of our current simulations, and thus we may overestimate microlens flux changes in the high-magnification tail for stars that are larger than the effective magnified Einstein radius of the microlenses. We aim to improve on this with higher-resolution calculations and with a star radius distribution of the giants and supergiants that are self-consistently predicted by the stellar synthesis models of the star formation history described above.
3. In terms of CDM-based subhalo models, we have only explored the canonical, reasonable choice for the subhalo mass function. A fuller exploration of subhalo parameter space includes the slope of the mass function and choices of the upper and lower mass limits. Also desirable would be more clarity regarding the effect of tidal stripping by the cluster, which has been hard to model with widely varying estimates given the N-body limitations given the wide dynamical range required to simulate the evolution of cluster substructure.
4. As constraints improve with increasing microlensing detections, we will need to consider the smoothing effect of baryons more carefully; in particular, the cluster gas may be expected to make a 5%–10% contribution to the column of matter at the Einstein radius, in addition to the estimated 1% from microlensed stars, which in the case of ψDM has been shown to slightly smooth the lensing corrugations, reducing the effective de Broglie scale (A. Amruth et al. 2023). This smoothing effect of ICL stars and cluster gas will also reduce the lensing amplitude of CDM subhalos as the perturbing deflection angles are reduced in proportion by the fractional contribution of isotropic, smooth mass components. Allowance is also needed for some variation in the momentum of the dark matter expected within A370 that may affect the de Broglie scale given the unfinished virialization state implied by the observed bimodality of A370, with hydrodynamical modeling indicating an ongoing major merger viewed after two core passages (K. Umetsu et al. 2022). For ψDM, some allowance may also be made for the presence of massive cluster members as the de Broglie scale is larger, scaling as $M_{\rm halo}^{-1/3}$ (H.-Y. Schive et al. 2014), depending on the column density of the member galaxy

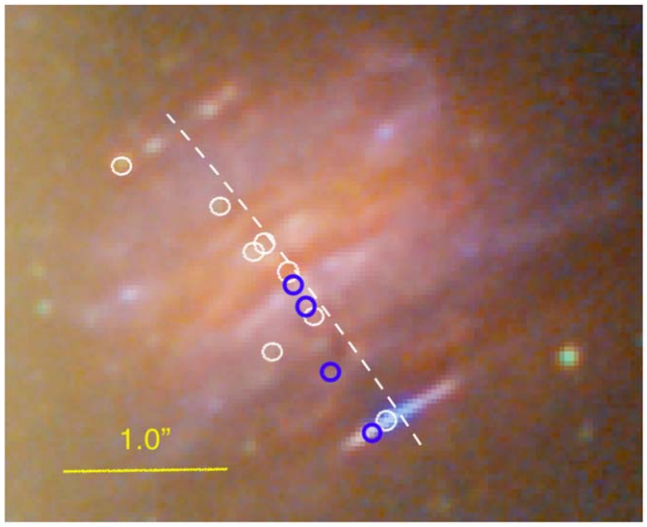

Figure 6. Microlensed stars detected by JWST in this multiply lensed galaxy ($z = 0.94$) behind the massive cluster MACS0416 ($z = 0.397$), repeatedly observed by the PEARLS team (H. Yan et al. 2023; R. A. Windhorst et al. 2023), marked as white circles, with an additional transient star detected by HST "Warhol" (W. Chen et al. 2019; bottom white circle). A further four new microlensed blue giants have been identified in our Flashlights/HST program (P. L. Kelly et al. 2022), shown as blue circles. The mirror symmetry is very clear and reveals that all 12 microlensed stars favor the left side of the lensed galaxy, following the "inside" of the tangential critical curve (dashed white line), with offsets on the subarcsecond scale like the Dragon Arc.

relative to that of the cluster, causing the overall width of the microlensing band to expand locally, scaling as $\sqrt{\lambda_{\rm dB}}$.

Deeper imaging of the Dragon Arc with a monthly cadence can uncover an order of magnitude more microlensing events per year, with deeper imaging to reach into the RGB population, as shown in Figure 2. Such data can reveal the fine structure of any network of critical curves, in particular any relatively large CDM-like subhalos with their individual Einstein rings, as can be seen in Figure 4. Radially elongated corrugations and island critical curves of ψDM may then be visible directly, with sufficient numbers of microlenses, particularly for a larger de Broglie wavelength. If, with more data, a featureless band is found, this would indicate microlensing by uniform, compact objects such as primordial black holes (PBH) or other compact microlensing objects, especially if a prominent central band along the critical curve is seen, as predicted in Figure 3. The light curves can help, as high-frequency, small-flux modulations on a daily timescale can distinguish PBH from the smoother variation predicted by a lower level of stellar microlensing modulated by CDM or ψDM substructure. The color of the microlensing stars can also help distinguish positive from negative parity regions to identify the precise location of the cluster critical curve as the more magnified events along the inside of the critical curve reach further into the RGB, where the lower-luminosity stars are somewhat bluer. It should also be possible to see the corrugated pattern of critical curves for low-redshift images lensed by massive galaxies, as the lower momentum predicts a resolvable de Broglie scale of 100 pc, an order of magnitude larger than for cluster lensing. This predicted momentum dependence for ψDM contrasts with CDM, which is not expected to show a strong scale dependence, as the subhalo population is largely independent of the host lens.

Finally, we notice similar behavior in another low-redshift lensed galaxy ($z = 0.94$), the Jupiter Arc, shown in Figure 6, where clear mirror symmetry is visible in JWST images along this fold arc, allowing the path of the critical curve to be identified precisely and independently of lens model uncertainties. Seven microlensed stars have been detected in cadenced PEARLS team images with JWST of this massive lensing cluster target MACS0416 (R. A. Windhorst et al. 2023; H. Yan et al. 2023). Within this lensed galaxy, an additional microlensed star "Warhol" has been previously detected by HST (W. Chen et al. 2019) as well as four new FLASHLIGHT detections of blue giants. All 12 of these transients closely follow the inner edge of the critical curve, with offsets on the subarcsecond scale like the Dragon Arc, and the mirror symmetry here means the source star population is identical on both sides, thereby providing independent confirmation of the preference for negative parity microlensing identified here for the Dragon Arc.

Acknowledgments

We thank the anonymous referee for an insightful and stimulating report. T.J.B. and P.M. are supported by Basque government grant No. IT1628-22 and Spanish project grant PID2021-123226NBI00 funded by MCIN/AEI/10.13039/501100011033. P.M. also acknowledges financial support from the Donostia International Physics Center (DIPC) and fellowship PIF22/177 (UPV/EHU). P.M. thanks the Physics Department of Hong Kong University for their hospitality. S.K.L. and J.L. acknowledge the General Research Fund under grant RGC/GRF 17312122, which is issued by the Research Grants Council of Hong Kong S.A.R. T.J.B., S.K.L., J.L., T.L., and G.S. acknowledge support by the Collaborative Research Fund under grant No. C6017-20G, which is issued by the Research Grants Council of Hong Kong S.A.R. R.A.W. acknowledges support from NASA JWST Interdisciplinary Scientist grants NAG5-12460, NNX14AN10G, and 80NSSC18K0200 from GSFC. J.M.D. and J.M.P. acknowledge the support of project PID2022-138896NB-C51 (MCIU/AEI/MINECO/FEDER, UE) Ministerio de Ciencia, Investigación y Universidades. A.Z. acknowledges support by grant No. 2020750 from the United States–Israel Binational Science Foundation (BSF) and grant No. 2109066 from the United States National Science Foundation (NSF); by the Ministry of Science & Technology, Israel; and by the Israel Science Foundation grant No. 864/23. L.L.R.W. acknowledges the support of NASA grant HST-SNAP-17504. This work was supported by JSPS KAKENHI grant Nos. JP23K22531, 20H05856, 22K21349, and JP22J21440.

ORCID iDs

Tom Broadhurst https://orcid.org/0000-0002-8785-8979
Sung Kei Li https://orcid.org/0000-0002-4490-7304
Amruth Alfred https://orcid.org/0000-0003-1276-1248
Jose M. Diego https://orcid.org/0000-0001-9065-3926
Paloma Morilla https://orcid.org/0009-0008-5791-1012
Patrick L. Kelly https://orcid.org/0000-0003-3142-997X
Fengwu Sun https://orcid.org/0000-0002-4622-6617
Masamune Oguri https://orcid.org/0000-0003-3484-399X
Hayley Williams https://orcid.org/0000-0002-1681-0767
Rogier Windhorst https://orcid.org/0000-0001-8156-6281
Adi Zitrin https://orcid.org/0000-0002-0350-4488
Katsuya T. Abe https://orcid.org/0000-0001-5474-4716
Wenlei Chen https://orcid.org/0000-0003-1060-0723

Liang Dai https://orcid.org/0000-0003-2091-8946
Yoshinobu Fudamoto https://orcid.org/0000-0001-7440-8832
Hiroki Kawai https://orcid.org/0009-0006-6911-2299
Jeremy Lim https://orcid.org/0000-0003-4220-2404
Tao Liu https://orcid.org/0000-0002-5248-5076
Ashish K. Meena https://orcid.org/0000-0002-7876-4321
Jose M. Palencia https://orcid.org/0000-0003-0942-817X
George F. Smoot https://orcid.org/0000-0001-7575-0816
Liliya L.R. Williams https://orcid.org/0000-0002-6039-8706

References

Abe, K. T., Kawai, H., & Oguri, M. 2024, PhRvD, 109, 083517
Amruth, A., Broadhurst, T., Lim, J., et al. 2023, NatAs, 7, 736
Arvanitaki, A., Dimopoulos, S., Dubovsky, S., Kaloper, N., & March-Russell, J. 2010, PhRvD, 81, 123530
Broadhurst, T. J., Taylor, A. N., & Peacock, J. A. 1995, ApJ, 438, 49
Carnall, A. C., McLure, R. J., Dunlop, J. S., & Davé, R. 2018, MNRAS, 480, 4379
Chan, J. H. H., Schive, H.-Y., Wong, S.-K., Chiueh, T., & Broadhurst, T. 2020, PhRvL, 125, 111102
Chen, S.-R., Schive, H.-Y., & Chiueh, T. 2017, MNRAS, 468, 1338
Chen, W., Kelly, P. L., Diego, J. M., et al. 2019, ApJ, 881, 8
Chen, W., Kelly, P. L., Treu, T., et al. 2022, ApJL, 940, L54
Dai, L. 2021, MNRAS, 501, 5538
Dai, L., Kaurov, A. A., Sharon, K., et al. 2020, MNRAS, 495, 3192
Dai, L., Venumadhav, T., Kaurov, A. A., & Miralda-Escude, J. 2018, ApJ, 867, 24
Diego, J. M., Kaiser, N., Broadhurst, T., et al. 2018, ApJ, 857, 25
Diego, J. M., Li, S. K., Amruth, A., et al. 2024, A&A, 689, A167
Diego, J. M., Meena, A. K., Adams, N. J., et al. 2023, A&A, 672, A3
Diego, J. M., Pascale, M., Kavanagh, B. J., et al. 2022, A&A, 665, A134
Diego, J. M., Sun, B., Yan, H., et al. 2023, A&A, 679, A31
Diego, J. M., Tegmark, M., Protopapas, P., & Sandvik, H. B. 2007, MNRAS, 375, 958
Doughty, C. C., Hennawi, J. F., Oñorbe, J., Davies, F. B., & Lukić, Z. 2023, arXiv:2312.01480
Fudamoto, Y., Sun, F., Diego, J. M., et al. 2024, arXiv:2404.08045
Furtak, L. J., Meena, A. K., Zackrisson, E., et al. 2024, MNRAS, 527, L7
Hartley, P., Jackson, N., Sluse, D., Stacey, H. R., & Vives-Arias, H. 2019, MNRAS, 485, 3009
Hosek, M. W. J., Lu, J. R., Lam, C. Y., et al. 2020, AJ, 160, 143
Hui, L. 2021, ARA&A, 59, 247
Hui, L., Ostriker, J. P., Tremaine, S., & Witten, E. 2017, PhRvD, 95, 043541
Iršič, V., Viel, M., Haehnelt, M. G., Bolton, J. S., & Becker, G. D. 2017, PhRvL, 119, 031302
Kawai, H., Oguri, M., Amruth, A., Broadhurst, T., & Lim, J. 2022, ApJ, 925, 61
Kelly, P. L., Chen, W., Alfred, A., et al. 2022, arXiv:2211.02670
Kelly, P. L., Diego, J. M., Rodney, S., et al. 2018, NatAs, 2, 334
Kelly, P. L., Rodney, S., Treu, T., et al. 2023, Sci, 380, 1322
Kelly, P. L., Rodney, S. A., Treu, T., et al. 2016, ApJL, 819, L8
Kroupa, P. 2001, MNRAS, 322, 231
Laguë, A., Schwabe, B., Hložek, R., Marsh, D. J. E., & Rogers, K. K. 2024, PhRvD, 109, 043507
Li, S. K., Kelly, P. L., Diego, J. M., et al. 2024, arXiv:2404.08571
Meena, A. K., Arad, O., & Zitrin, A. 2022, MNRAS, 514, 2545
Meena, A. K., Chen, W., Zitrin, A., et al. 2023a, MNRAS, 521, 5224
Meena, A. K., Zitrin, A., Jimé nez-Teja, Y., et al. 2023b, ApJL, 944, L6
Miralda-Escude, J. 1991, ApJ, 379, 94
Navarro, J. F., Frenk, C. S., & White, S. D. M. 1997, ApJ, 490, 493
Nhan Luu, H., Mocz, P., Vogelsberger, M., et al. 2024, MNRAS, 527, 4162
Niemeyer, J. C. 2020, PrPNP, 113, 103787
Niemiec, A., Jauzac, M., Eckert, D., et al. 2023, MNRAS, 524, 2883
Nierenberg, A. M., Gilman, D., Treu, T., et al. 2020, MNRAS, 492, 5314
Nierenberg, A. M., Keeley, R. E., Sluse, D., et al. 2024, MNRAS, 530, 2960
Oguri, M., Diego, J. M., Kaiser, N., Kelly, P. L., & Broadhurst, T. 2018, PhRvD, 97, 023518
Palencia, J. M., Diego, J. M., Kavanagh, B. J., & Martinez, J. 2023, A&A, 687, A81
Pascale, M., & Dai, L. 2024
Powell, D. M., Vegetti, S., McKean, J. P., et al. 2023, MNRAS, 524, L84
Pozo, A., Broadhurst, T., Smoot, G. F., et al. 2024, PhRvD, 109, 083532
Rodney, S. A., Balestra, I., Bradac, M., et al. 2018, NatAs, 2, 324
Rogers, K. K., & Peiris, H. V. 2021, PhRvL, 126, 071302
Schive, H.-Y., Chiueh, T., & Broadhurst, T. 2014, NatPh, 10, 496499
Schive, H.-Y., Liao, M.-H., Woo, T.-P., et al. 2014, PhRvL, 113, 261302
Sendra, I., Diego, J. M., Broadhurst, T., & Lazkoz, R. 2014, MNRAS, 437, 2642
Umetsu, K., Ueda, S., Hsieh, B.-C., et al. 2022, ApJ, 934, 169
Vall Müller, C., & Miralda-Escudé, J. 2024, MNRAS, in press
Venumadhav, T., Dai, L., & Miralda-Escudé, J. 2017, ApJ, 850, 49
Wagner, J. 2019, Univ, 5, 177
Weisenbach, L., Anguita, T., Miralda-Escudé, J., et al. 2024, arXiv:2404.08094
Welch, B., Coe, D., Diego, J., et al. 2022, Natur, 603, 815
Williams, L. L. R., Kelly, P. L., Treu, T., et al. 2023, ApJ, 961, 200
Windhorst, R. A., Cohen, S. H., Jansen, R. A., et al. 2023, AJ, 165, 13
Windhorst, R. A., Timmes, F. X., Wyithe, J. S. B., et al. 2018, ApJS, 234, 41
Yan, H., Ma, Z., Sun, B., et al. 2023, ApJS, 269, 43
Zhu, Y., Becker, G. D., Bosman, S. E. I., et al. 2022, ApJ, 932, 76
Zimmermann, T., Alvey, J., Marsh, D. J. E., Fairbairn, M., & Read, J. I. 2024, arXiv:2405.20374
Zitrin, A., & Broadhurst, T. 2009, ApJL, 703, L132